Using ambient seismic noise to image the mantle transition zone

Master thesis by Imme Wienk
Supervisors: Prof. dr. Arwen Deuss and dr. Hanneke Paulssen

March 15, 2024

Abstract

Imaging of the mantle transition zone, the part of the Earth's mantle bound by the 410 and 660 km discontinuities, has long been confined to earthquake data only. Recent studies demonstrated that the mantle transition zone can also be imaged with seismic interferometry, a method to approximate the Green's function between receiver pairs by cross-correlating ambient seismic noise. Retrieving body waves that have travelled through the deep Earth with this method remains challenging, because surface waves are the dominant signals in ambient seismic noise records. Our study investigates if mantle transition zone reflections can be observed in California, using ambient seismic noise. Four years of seismic data (2018–2021) for 251 stations is retrieved, preprocessed, cross-correlated and stacked in variable time windows. The results are dependent on many factors, such as frequency range, season and interstation distance. The mantle transition zone reflections are best observed between June and August, because in these months useful microseismic noise is generated in the Southern Ocean, close to the antipode of the array. The frequency range giving the best reflections is 0.07–0.15 Hz, including both the primary and secondary microseisms.

Contents

1 Introduction

The Earth's mantle contains two main seismic discontinuities. Around 410 and 660 km depth, seismic velocities rapidly increase over a narrow depth interval. These discontinuities separate the upper from the lower mantle and form the mantle transition zone. The sharp velocity gradients are generally interpreted to be generated by pressure-induced polymorphic phase transitions in the mineral olivine. (Helffrich & Wood, 2001). The 410 km discontinuity is the result of a transition from olivine to wadsleyite and the 660 km discontinuity is caused by the transition of ringwoodite into bridgemanite and magnesiowüstite. The characteristics of the mantle transition zone discontinuities play a key role in mantle dynamics. The 660 km discontinuity strongly influences mantle convection, determining the fate of subducted slabs (Li et al., 2008). The 410 km discontinuity may provide constraints on the potential existence of fluids in the mantle (Deuss, 2009). Seismology plays a major role in providing measurements of elastic properties of the Earth's mantle.

Many approaches have been taken for investigating the 410 and 660 km discontinuities. Imaging techniques mostly rely on earthquake observations, such as SS-precursors (Shearer & Masters, 1992), receiver functions (Chevrot et al., 1999), PP-precursors (Benz & Vidale, 1993) and ScS reverberations (Revenaugh & Jordan, 1991). Earthquake based imaging methods are limited by the geographical distribution and specific time windows of earthquakes and the uncertainties of earthquake source parameters associated with the complex rupture process.

In the 2000s, seismologists found that ambient seismic noise can also contain useful information about the Earth's interior. Ambient seismic noise is a seismic signal that is always present. It is a background signal continuously observed at relatively low, fluctuating amplitudes, on seismic stations worldwide (Reading et al., 2014). Ambient seismic noise can originate from different sources. Below 1.0 Hz seismic noise is primarily caused by nature. Seismic noise with frequencies below 0.003 Hz is mainly controlled by atmospheric processes (Sorrells et al., 1971). Between 0.003 Hz and 1.0 Hz the dominant causes are processes in the oceans (Tanimoto & Anderson, 2023). This range is often called the microseism range. Microseisms are generated by interactions between ocean waves and the solid Earth (Boué et al., 2013). In the absence of earthquakes, they are the largest signal in seismograms (Tanimoto et al., 2006). They are categorized into primary and secondary microseisms, visible in seismic noise spectra as two prominent peaks around 0.05–0.12 and 0.1–0.25 Hz, respectively (Gerstoft et al., 2008). The primary microseisms originate from direct coupling of strong oceanic waves and the seafloor (Landès et al., 2010). Secondary microseisms are characterized by stronger amplitudes and are produced at double the frequency of primary microseisms by a nonlinear interaction of oceanic waves propagating in opposite directions. The pressure exerted on the ocean floor can be approximated by vertical forces that dominantly generate P-waves (Nishida & Takagi, 2016). Noise above 1.0 Hz is primarily anthropogenic of origin but is also affected by local weather conditions (Peterson, 1993).

The approach using ambient seismic noise for investigating the Earth's subsurface is called seismic interferometry. Seismic interferometry computes cross-correlations between seismic data of receiver pairs. Cross-correlation is a time dependent measure of similarity between two signals where one is shifted relative the other. In other words, at the maximum correlation it gives the time delay between the two signals. Theoretically, when noise sources are distributed homogeneously in space, the resulting signal can be interpreted as the impulse response (Green's function) between two receivers, where one of the receivers acts as a virtual delta source (Wapenaar et al., 2010). In practice this requirement is not met leading to differences between the cross-correlation and the Green's function (Tkalčić et al., 2020).

As seismic noise sources are located at Earth's surface, noise correlations are dominated by surface waves. Shapiro & Campillo (2004) were the first to extract intermediate and

long period surface waves from field data. In the last decade, surface waves extracted from ambient noise cross-correlations have been widely used to investigate the crustal and upper mantle structure (e.g. Sabra et al. (2005); Yao & Van Der Hilst (2009); Lin et al. (2009)).

Surface waves have limited depth resolution and are therefore not sufficient to investigate the mantle transition zone. Instead, body waves that have travelled through the deep earth are required. Body-wave extraction from noise correlations is a greater challenge than surface-wave extraction. Firstly because of the dominance of Rayleigh waves due to the excitation at the surface. Secondly, amplitudes decay more rapidly with distance making the signals harder to detect. The signal-to-noise ratio generally increases with stacking over long time windows and a large number of stations. With the deployment of dense seismic arrays and with the use of these stacking strategies, body waves have been successfully observed on different scales (Gerstoft et al., 2008). Roux et al. (2005) identified direct P-waves from noise cross-correlations on the very local scale, using one month of seismic noise data for 30 seismic stations located in an 11-km square. Although with much weaker amplitudes than the dominant surface waves, more and more body wave signals have been identified with seismic interferometry. Zhan et al. (2010), Ruigrok et al. (2011) and Poli et al. (2012b) all found body waves in noise correlations at the crustal scale.

Poli et al. (2012a) was the first study that used body wave signals from ambient seismic noise to investigate the deeper Earth. They studied the mantle transition zone below the Fennoscandian Shield, a part of the East European Craton in northern Finland. The study computed and stacked cross-correlations in the microseism range (0.1–0.5 Hz) and extracted P wave signals reflected on the 410 and 660 km discontinuities, demonstrating that mapping of the mantle transition zone is possible without using earthquake sources. More studies have extracted body waves reflected on discontinuities from ambient seismic noise in the microseism range since then. Feng et al. (2017) used a dense seismic array in eastern North China to recover reflected P wave signals from the 410 km and 660 km discontinuities with ambient noise cross-correlations. They applied phase-weighted stacking (Schimmel & Paulssen, 1997) as well as linear stacking. A follow-up study showed clear reflected body wave signals from the transition zone discontinuities with significant lateral variations (Feng et al., 2019). A third study combined the body waves reflected at the 410 and 660 km discontinuities retrieved from ambient noise with mineral physics modeling (Feng et al., 2021). Similar to Poli et al. (2012a), all three above mentioned studies used seismic arrays located on a craton, the North China Craton. Cratons are regions of continental lithosphere that have remained largely undeformed since the Archaean (Hoffman, 1988). Cratons are ideal for seismic interferometry because of their homogeneous velocity structure. This causes time delays at receivers to be primarily caused by differences in travel distance and not by local variations in the velocity structure. Lu et al. (2023) showed that it is also possible to map the mantle transition zone discontinuities beneath South-Central Europe with ambient seismic noise, which is not located on a craton.

The aim of this study is to investigate if mantle transition zone reflections can also be observed in a more heterogeneous non-craton region using ambient seismic noise. Applying this method to a new area will add new insights to the method and can possibly help improve it. California is chosen as location because it has a dense seismic network and complete data availability.

2 Data

To retrieve mantle transition zone reflections, waves with near vertical incident angles are preferred because these waves have travelled through the deep Earth. Mainly PKP and PKIKP waves meet this criterion and they are generated near the antipode of the array. Figure 1 shows why these core phases are preferred: they focus towards the seismic array, increase in amplitude, and different source regions can lead to the same incident angle. The seismic array used in this study should therefore have an ocean located at the antipode, as this is where microseismic noise is generated. California is chosen as location because it has an antipode located in the Southern Ocean. Also, the Southern California Seismic Network (SCSN) is a dense network (Figure 2) and has a complete data record. The seismic data are downloaded from the Southern California Earthquake Data Center (California Institute of Technology and United States Geological Survey Pasadena, 1926). Four years of continuous seismic data is collected between January 2018 and December 2021 for 251 broadband (BHZ) stations. Only the vertical component is used and all data is cut into daily segments for preprocessing.

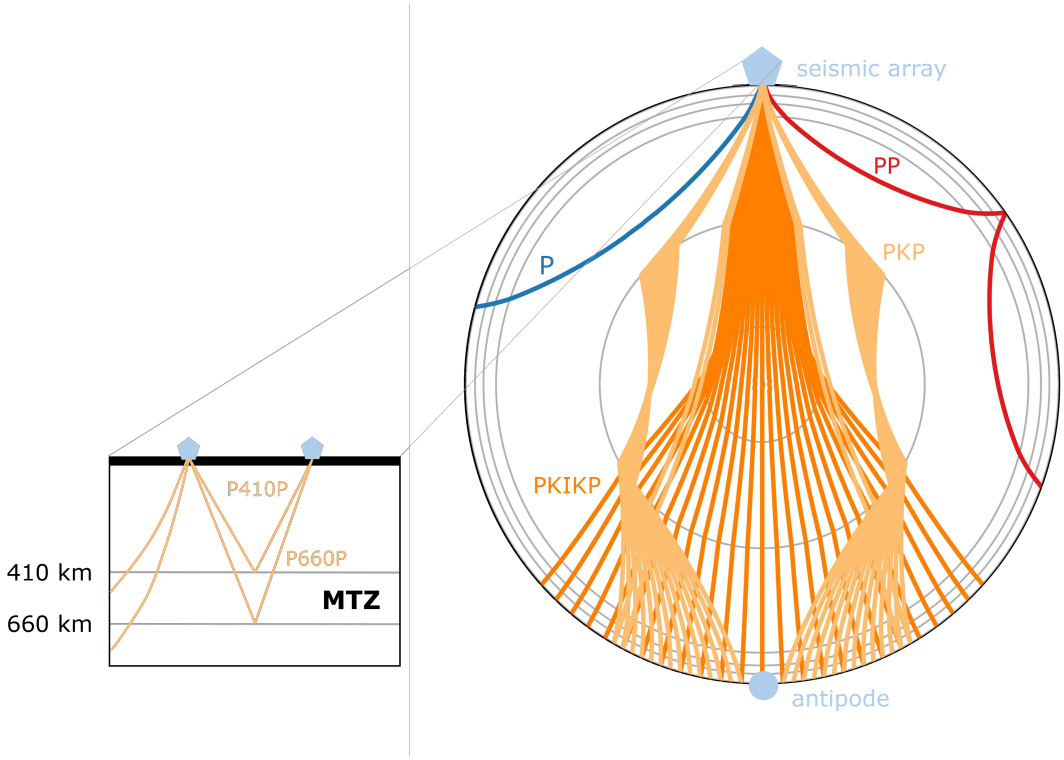

Figure 1: Different P wave types that can be used in this study. Pentagon gives location of seismic array, circle gives location of the antipode. Core phases originating around the antipode focus at the seismic array. Enlarged part shows wave paths of the P410P and P660P at the seismic array. MTZ = mantle transition zone.

3 Methods

The methods of this study can be divided into three distinct phases: preproccessing, computing cross-correlations and different forms of stacking. A schematic flow chart of the different steps is given in Figure 3. The next sections will describe each phase in detail.

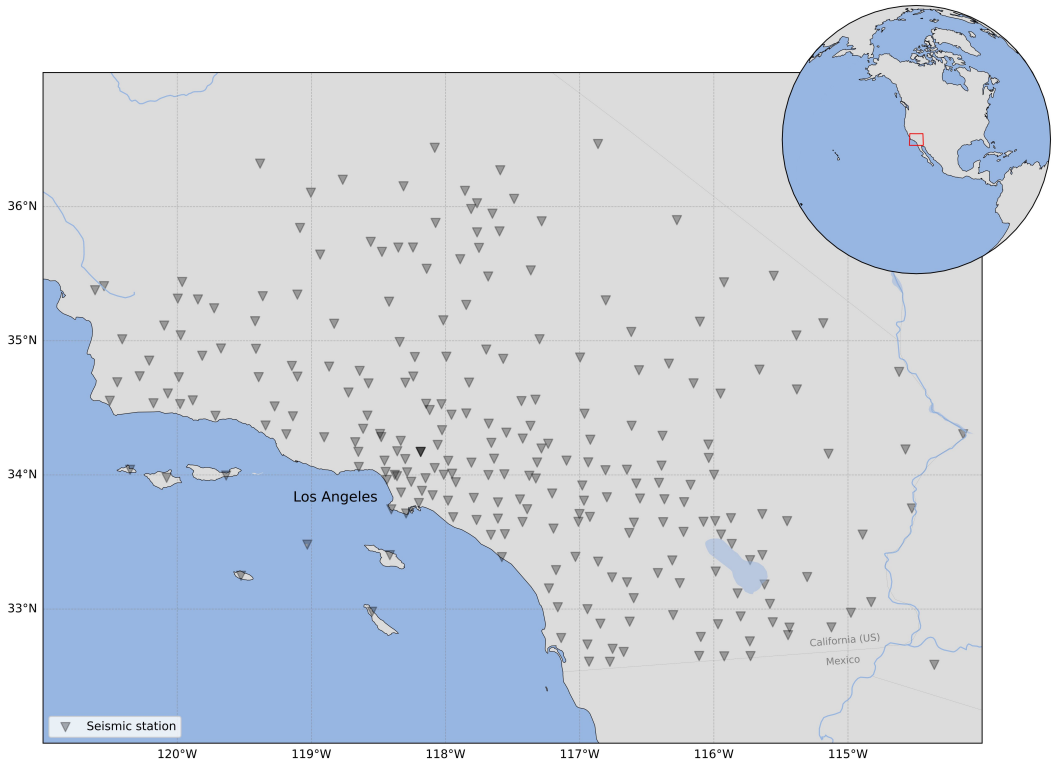

Figure 2: Southern California Seismic Network showing all 251 seismic stations used in this study .

3.1 Data processing

Before any cross-correlations can be made, the data should be properly processed. The preprocessing steps are based on Bensen et al. (2007) and applied on a single day of data for each station individually. To account for problems at signal edges that can occur in the preprocessing routine, the daily segments have two extra minutes added at the beginning and the end of the day. These two minutes are removed at the end of the preprocessing routine, resulting in a properly processed daily segment. The first steps of the preprocessing routine are: resampling, removal of data mean and trend and removing the instrument response. The retrieved data have a sampling rate of 40 Hz and will be downsampled to 5 Hz. The preprocessing described in Bensen et al. (2007) has no resampling. However, in this research, the recorded sampling rate of 40 Hz is superfluous and can cause problems in storage and computational time. The Nyquist–Shannon sampling theorem states that to avoid aliasing the sample rate must be at least twice the bandwidth of the signal:

$$f_n \leq \frac{1}{2}\Delta t \tag{1}$$

Here, f_n is the Nyquist frequency and Δt the sampling rate. The maximum frequency considered here is 1 Hz (highest frequency in the microseism range), giving a minimum sampling rate of 2 Hz. To keep a safe margin the data is downsampled to 5 Hz. The data is then demeaned and detrended. The retrieved seismograms are expressed in counts, showing digitized versions of the displacement convolved with the instrument response. To get the displacement, deconvolution of the instrument response is performed. The output trace is bandpassed as the deconvolution process can be unstable and introduce high amplitude output signals or low amplitude input signals at high frequencies. This wide bandpass filter is between 0.02 Hz and 2.4 Hz.

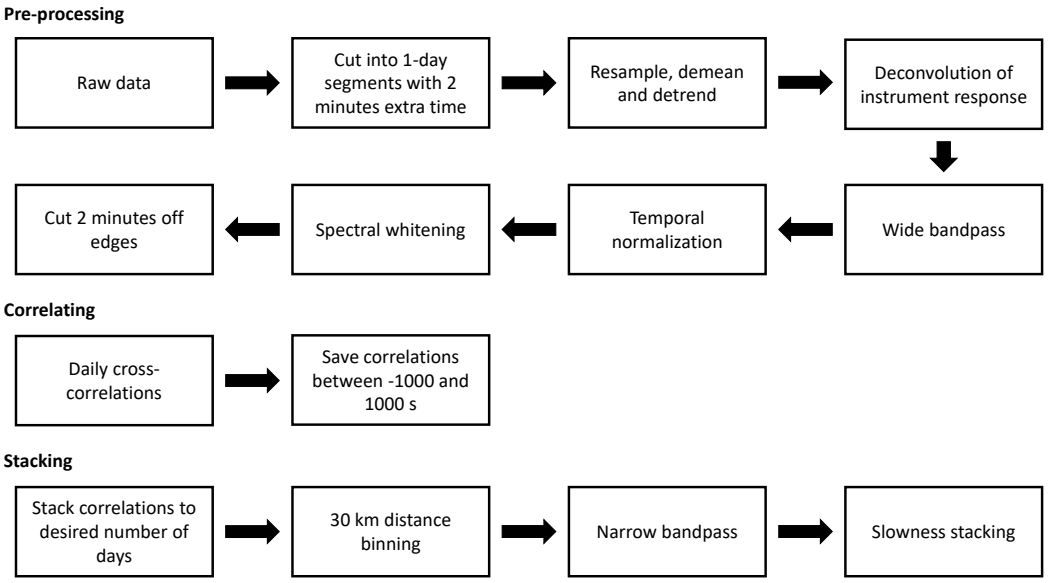

Figure 3: Flowchart of the three distinct phases used in the methods of this study.

3.1.1 Temporal normalization

The most important step in the data processing is temporal normalization, a procedure for reducing the effect of instrumental errors, earthquakes and non-stationary noise sources near stations. Bensen et al. (2007) described five different approaches to temporal normalization: one-bit normalization, applying a clipping threshold equal to the root-mean-square amplitude of the signal, normalization involving automated event detection, running-absolute-mean-normalization and water-level normalization. Their study shows that one-bit, running-absolute-mean and water-level normalization all produce similar results. However, water-level normalization is an iterative approach and therefore time consuming. They prefer running-absolute-mean-normalization over one-bit normalization because of its greater adaptability to the data. We therefore used the running-absolute-mean-normalization. This approach computes the running average of the absolute value of the waveform in a time window of fixed length and weights the waveform at the centre of the window by the inverse of this average:

$$\hat{d}_n = \frac{d_n}{w_n} \quad \text{where} \quad w_n = \frac{1}{2N+1} \sum_{j=n-N}^{n+N} |d_j| \tag{2}$$

Here, d_n is the input data, w_n is the weighing factor and $\hat{d}_n$ is the normalized data. The width of the normalization window $2N+1$ determines how much information on the amplitude is retained. Bensen et al. (2007) determined that about half the maximum period of the signal works well. The weights are computed on the bandpassed waveform data leading to a window of 100 seconds. The running-absolute-mean-normalization gives perturbed results at the edges of the signal, as no complete window is present. However, as it falls into the 2 minute range that will be cut at the end of the preprocessing routine, this will have no effect on the final daily segments.

3.1.2 Spectral whitening

Seismic noise is not spectrally white, it does not have a flat amplitude spectrum. The amplitude spectrum shows two peaks at the primary (around 15 s) and secondary (around 7.5 s)

microseisms, these peaks are shown in an example of an amplitude spectrum in Figure 4a. To diminish the relative dominance of the microseism peaks the data should be spectrally whitened. This is done by dividing the original spectrum by a smoothed version of the amplitude spectrum. This way the phase information is retained but amplitudes are smoothed. An example of a white spectrum is given in Figure 4b. As this process is done in the frequency domain, an inverse Fourier transform is applied to return the signal back to the time domain.

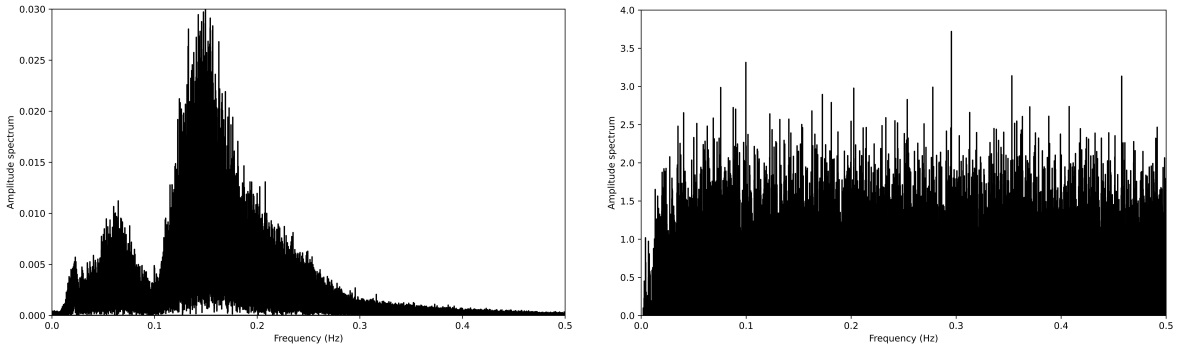

(a) Amplitude spectrum before whitening.

(b) Amplitude spectrum after whitening.

Figure 4: Example of amplitude spectrum before and after whitening. Before whitening the spectrum shows the primary and secondary microseism peaks. After whitening the spectrum is flat. Data is from station TUQ from 07-01-2018.

3.2 Cross correlations

After the preprocessing routine is completed, each station has four years of preprocessed data as daily segments. The next step is cross-correlating these daily segments for all possible station pairs. Cross-correlation computes the time delay between signals from two receivers. In a diffuse wavefield, where sources are distributed homogeneously around the receiver pair, the cross-correlation can be interpreted as an approximation of the impulse response between the two receivers, as if one of the receivers acts as a virtual delta source (Draganov et al., 2009). The assumption of a diffuse wavefield is often unrealistic which results in cross-correlations being different from the Green's function. The cross-correlation is given by:

$$(f \star g)(t) = \int_{-\infty}^{+\infty} f(\tau) g(\tau + t) d\tau \tag{3}$$

where f is the signal recorder at one receiver and g is the signal recorded at the other receiver. t represents the time lag and τ time. The result of the cross-correlation is a two-sided time function with both positive and negative times, where the positive part is called the causal part and the negative part the anticausal or acausal part. The causal part represents a positive time shift and the acausal part represents a negative time shift. Cross-correlation is not commutative, the order of the operands f and g determines which parts of the correlation become causal and acausal (Suslick, 2001). The signal from the most western station is taken as the first argument in the cross-correlation. The causal part then contains waves travelling from east to west and the acausal part are waves travelling in the opposite direction. Whereas the correlations originally have a length of twice the input signal (two days), they are saved from -1000 to 1000 s so they will not take up too much storage. To enhance the body waves each correlation is normalized with its maximum. The routine of Bensen et al. (2007) compresses the two-sided cross-correlation into a one-sided one by averaging the causal and acausal parts, arguing that this increases signal-to-noise ratio. In this study this is not done because it is interesting to see the differences between the causal and acausal parts first.

Cross-correlation is performed in the frequency domain because it is faster than in the time domain.

3.3 Stacking

3.3.1 Temporal stacking

Because seismic noise is a very weak ground motion and noise sources are inhomogeneous in time and space, temporal stacking over a long time range is required to get a good approximation of the Green's function (Stehly et al., 2006). This has proven to be effective for the retrieval of surface waves. All daily cross-correlations are therefore stacked into a four year stack containing all correlations. Body waves are less energetic than surface waves and therefore harder to detect with ambient seismic noise. Therefore, additional considerations are taken into account to detect them. Lu et al. (2022) used global mean ocean wave height data to show that the intensity of the microseismic noise field has a seasonal dependence. For this reason the correlations are also obtained as seasonal stacks. The stacking procedure consists of adding all daily correlations for a station pair that fall in the desired season and dividing by the amount of days that went into the stack, which differs per station pair. The linearity of cross-correlation guarantees that stacking daily cross-correlations produces the same result as cross-correlation applying to the longer time-series.

3.3.2 Distance binning

To further enhance the signal-to-noise ratio, distance binning is applied. First, the time stacks are arranged per interstation distance. Then, the average of all cross-correlations that fall in a 30 km wide distance bin is taken. The first bin thus takes the average of all cross-correlations between 0 and 30 km interstation distance. Each following bin is shifted 1 km with respect to the previous bin, resulting in 29 km overlap between the bins. The second bin therefore averages all the cross-correlations between 1 and 31 km. This procedure is continued until the maximum interstation distance is reached. By taking the average of these bins, coherent signals will add up constructively while incoherent signals will add up destructively.

3.3.3 Frequency dependence

After the binning procedure, a narrow bandpass filter is applied for multiple frequency ranges: 0.05–0.12 Hz (primary microseism range), 0.07–0.15 Hz, 0.09–0.17 Hz (in between the two microseism ranges) and 0.1–0.2 Hz (secondary microseism range).

3.3.4 Slowness stacking

To determine the incident angle of the incoming wavefront, slowness stacking is used. Determining this angle helps identifying the wave type (Figure 1) of the wavefront. Slowness is the inverse of the apparent velocity and is thus dependent on the incident angle. A slowness stack, or slant stack, estimates the seismic energy arriving at the array for different horizontal slownesses (Rost & Thomas, 2002). The process spatially stacks the cross-correlations for different slownesses. According to their interstation distance and the used slowness the cross-correlations are shifted in time, as given in Equation (4) below.

$$s_u(t) = \frac{1}{M} \sum_{i=1}^{M} cc_i(t - t_{u,i}) \quad \text{where} \quad t_{u,i} = x_i u \tag{4}$$

Here, $s_u(t)$ is the slant stack for slowness u. It is computed by summing cross-correlations $cc_i(t)$ that are shifted in time t according to $t_{u,i}$, the relative travel time between the receiver pairs for slowness u and interstation distance x_i and dividing by M, the number of receiver pairs.

4 Results

This section will show the results of stacking all computed cross-correlations for different stacking intervals and frequency ranges. The stacking intervals include all four years of data (Section 4.1) and the different seasons (Section 4.2). A slant stack is also given in Section 4.3.

4.1 Four year stack

Figure 5 shows stacks containing all four years of cross-correlations for the different frequency ranges: 0.05–0.12 Hz, 0.07–0.15 Hz, 0.09–0.17 Hz and 0.1–0.2 Hz. All correlations are arranged by interstation distance on the vertical axis. The horizontal axis shows the negative times of the acausal part and the positive times of the causal part of the correlations.

The general pattern of these figures mainly shows two wave types: surface waves and direct body waves. The most prominent arrivals are surface waves, as annotated in the figure. These arrivals are surface waves because as the interstation distance increases, the time difference increases with an apparent velocity of 3 km/s, corresponding to the velocity of surface waves (Ammon et al., 2020). Also, they are more evident for the lower frequency ranges and have high amplitudes (the scale bar of Figure 5 is clipped to enhance body wave arrivals). Since only the vertical component is used in these correlations, they must be Rayleigh waves. They are more prominent in the acausal parts of the correlations, which agrees with the dominant surface waves travelling from west to east in California (Tanimoto et al., 2006).

The second wave types observed in all frequency ranges are near zero time arrivals. Time differences are smaller with interstation distance than for the surface waves. These waves travel with an apparent velocity of 20 km/s, giving a slowness of 0.05 s/km. This corresponds with either a P wave with an epicentral distance of 75° or a PP wave with an epicentral distance of 150° (Wang et al., 2018a). For the two lower frequency ranges (Figures 5a and 5b) they only appear in the acausal part of the correlations, but for the higher frequencies (Figures 5c and 5d) they are visible in both the acausal and the causal parts.

The mantle transition zone reflections are expected at around 100 seconds for the P410P and 150 seconds for the P660P, corresponding to the vertical two way travel times of these waves. If they travel mostly vertically, the time difference should be similar for all interstation distances. In the first two frequency ranges (Figures 5a and 5b) it is impossible to observe the P410P at 100 seconds because of the excessive presence of surface waves. For the higher frequency ranges (Figures 5c and 5d), the surface waves are diminished at 100 seconds but the P410P is still not observed. Because the P660P is expected to arrive at 150 seconds it does not interfere with surface waves. Nevertheless it is not visible in any of the frequency ranges.

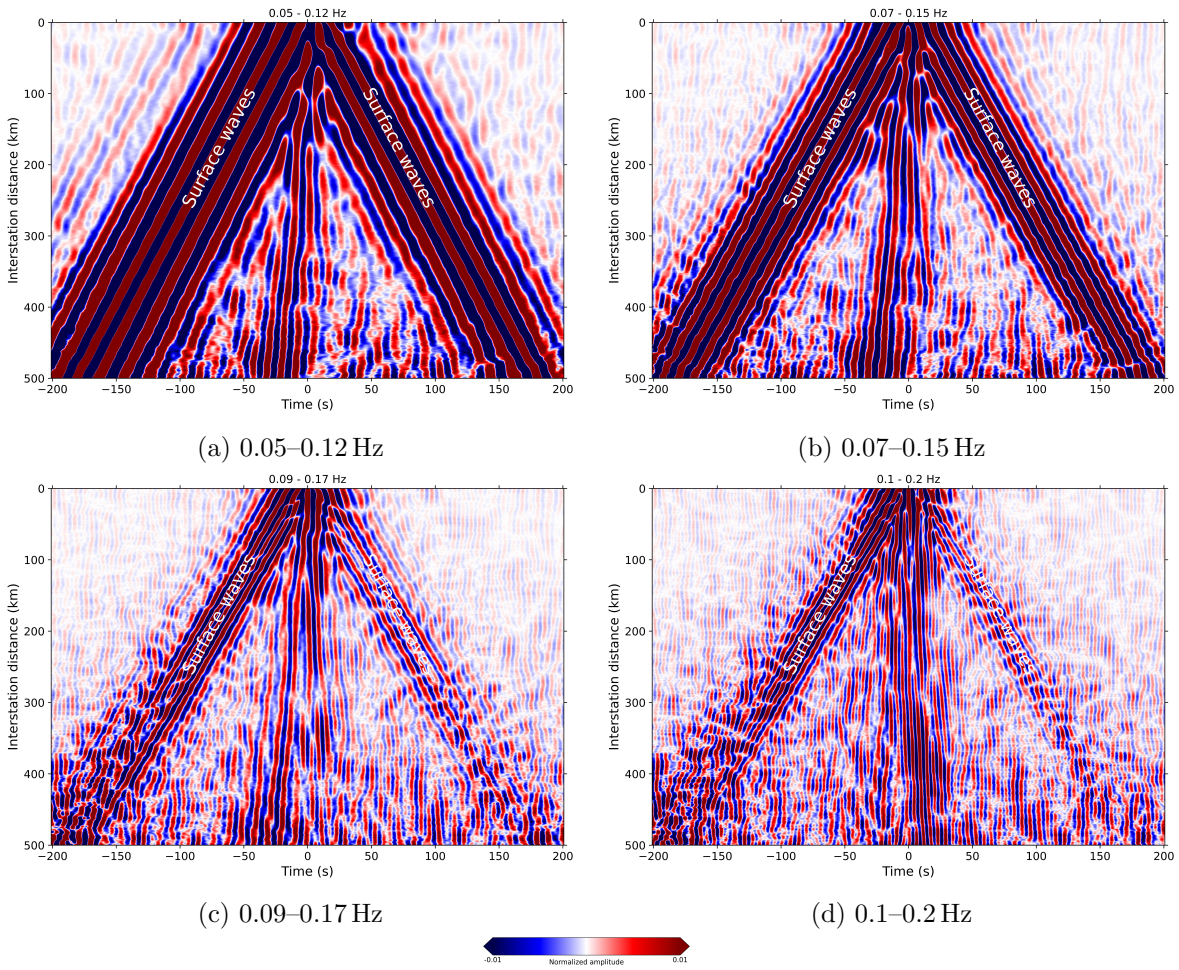

(a) 0.05–0.12 Hz

(b) 0.07–0.15 Hz

(c) 0.09–0.17 Hz

(d) 0.1–0.2 Hz

Figure 5: Data stacks containing all cross-correlations from four years of data (2018–2021) for different frequency ranges in both the primary and secondary microseism range. Vertical axis shows interstation distance, horizontal axis shows times negative and positive times corresponding with the acausal and causal part of the correlations, respectively. Neither of the stacks show mantle transition zone reflections.

4.2 Seasonal stacks

The intensity of microseismic noise shows seasonal variations, caused by variations in ocean wave height (Wang et al., 2018b). High ocean wave heights cause high microseismic noise intensities and can be regarded as local sources for microseismic noise. Global mean ocean wave height is thus a first-order estimate of the microseismic noise intensity.

Figure 6 shows global mean ocean wave height for the spring months (March, April, May), the summer months (June, July, August), the autumn months (September, October, November) and the winter months (December, January, February) of 2022. Seasonal variation is clearly visible: winter storms on the southern hemisphere cause high wave heights on the Southern Ocean between June and August (Figure 6b). In these months most microseismic noise will be generated close to the antipode of the array. Also, the Pacific Ocean is calm in these months, suggesting that few horizontally traveling surface waves are created close to the seismic array. This is favourable for detecting the P410P because too many surface waves interfere with this reflection.

Between December and February (Figure 6d), the situation is reversed. At the antipode of the array it is now summer resulting in a calm Southern Ocean which will generate little

microseismic noise. Close to the array, the Pacific Ocean is now experiencing winter storms leading to many horizontally travelling surface waves. The spring (Figure 6a) and autumn months (Figure 6c), are a transition between the end member situations of the summer and winter. Because most noise is generated at the antipode and few surface waves are created in summer, it is expected that the best results will be achieved in this season.

To investigate this, stacks are made for each season and for the same frequency ranges as for the stack containing all data. The complete set of figures can be found in Appendix A. Figure 7 only shows the 0.07–0.15 Hz frequency range, because this is where the best results are obtained. Surface waves dominate the stacks for the lowest frequency range (0.05–0.12 Hz). In the higher frequency ranges no clear arrivals at 100 or 150 seconds are observed.

Figure 7 shows that surface waves are visible in all seasonal stacks, with highest amplitudes in winter and lowest in the summer months. The direct P waves are also observable in all seasons, mostly in the acausal part, but in the summer stack they also appear in the causal part. Possible mantle transition zone reflections are visible in the causal parts of the spring and summer stacks. For the spring months there are two stable arrivals around 120 and 160 seconds, independent of interstation distance. The summer stack shows arrivals independent of interstation distance around 100 and 150 seconds, which could be the P410P and P660P reflections.

Figure 8 compares the first 100 km of the causal parts of the summer and winter stacks to determine whether the P410P and P660P reflections are larger than the surrounding signals. The single trace shows the average of all the cross-correlations with interstation distances up to 100 km. The summer stack shows a prominent arrival around 100 seconds and a slightly less prominent one around 150 seconds. The winter stacks shows no prominent arrivals.

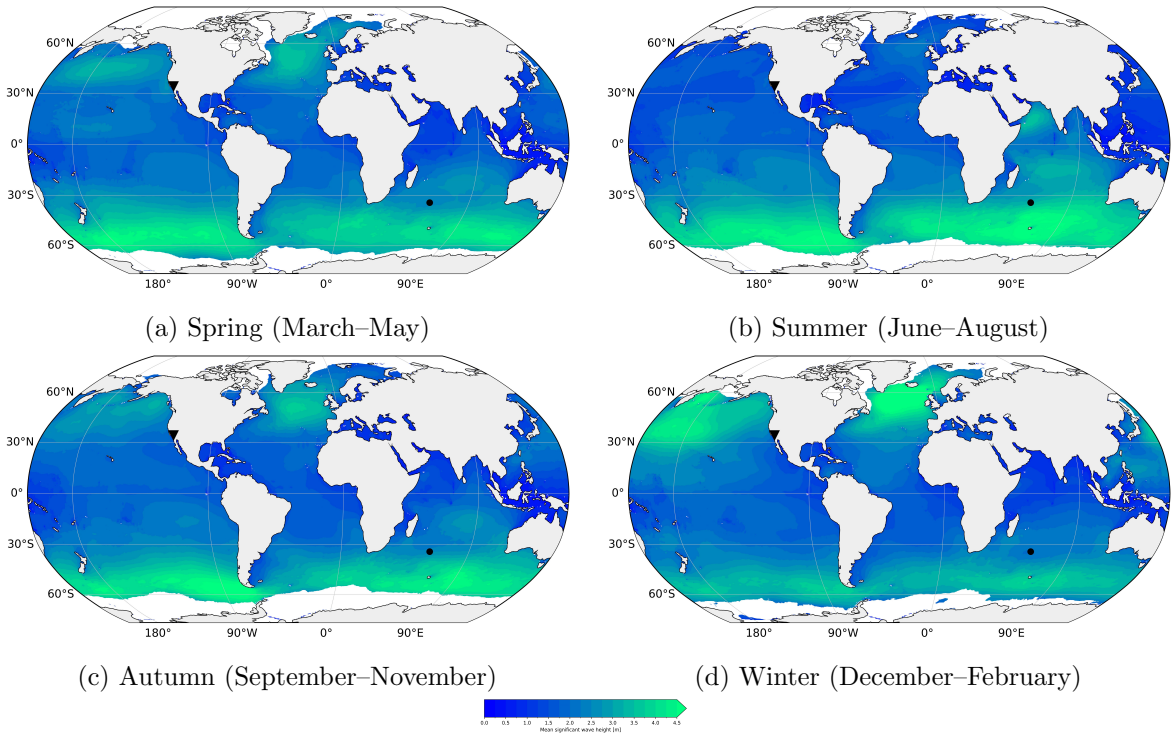

(a) Spring (March–May)

(b) Summer (June–August)

(c) Autumn (September–November)

(d) Winter (December–February)

Figure 6: Mean significant wave height over the seasons of 2022. The seismic array is located at the triangle. The antipode of the array is located at the circle. Data are downloaded from the E.U. Copernicus Marine Service Information (CMEMS, 2024). The sea surface wave significant height is downloaded in 12 hour windows between December 2021 and November 2022.

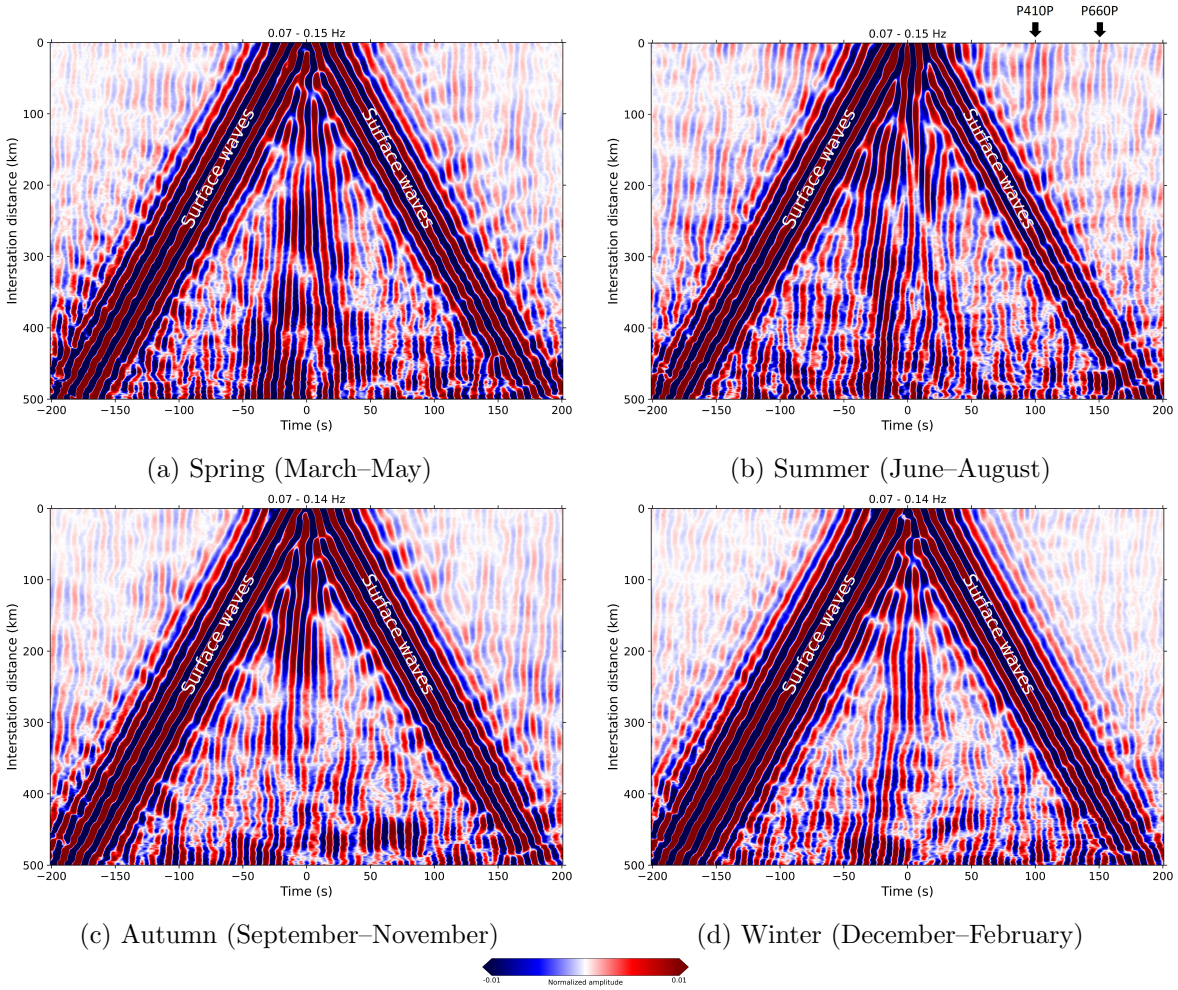

Figure 7: Seasonal data stacks of the cross-correlations arranged by interstation distance on the vertical axis for the frequency range 0.07–0.15 Hz. Best mantle transition zone reflections are observed in summer.

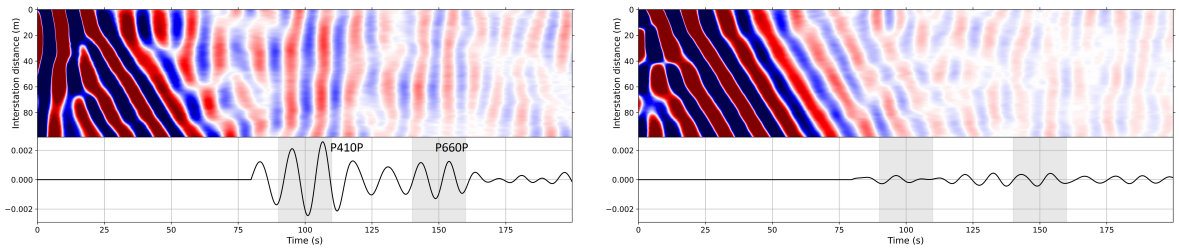

Figure 8: Close up of the first 100 km of the causal part of the total stack with averaged signal. Times where surface waves arrive (< 80 s) are set to zero in the averaged signal. Grey background shows expected arrivals of the mantle transition zone reflections.

4.3 Slant stack

To investigate the incident angle of the observed mantle transition zone reflections, a slant stack is made. Because the mantle transition zone are best visible in the summer stack for the first 100 km of the causal part, this is taken as input for the slant stack. Figure 9 shows this slant stack, giving the summed signal as in Figure 8a for different slownesses. The

stack clearly shows the wave trains arriving around 100 and 150 seconds, with the P410P more evident. The peak amplitudes are not at zero slowness, but around 0.027 s/km, which indicates a wavefront with an inclined angle. This slowness is in agreement with observations made in the data stack, because the arrival times of the mantle transition zone reflections in Figure 8a are not completely independent of interstation distance. In both the acausal and causal part the time delays of the reflections changes slightly for larger interstation distances.

Remarkable is that almost all signals in Figure 7b are tilted with the same angle and direction in both the acausal and causal parts of the correlations. In the acasual part it is as expected: as the interstation distance increases, the time difference increases as well. But in the causal part the situation is reversed: as the interstation distance increases, the time difference decreases. This is an unexpected result and will be further explored in the discussion (Section 5).

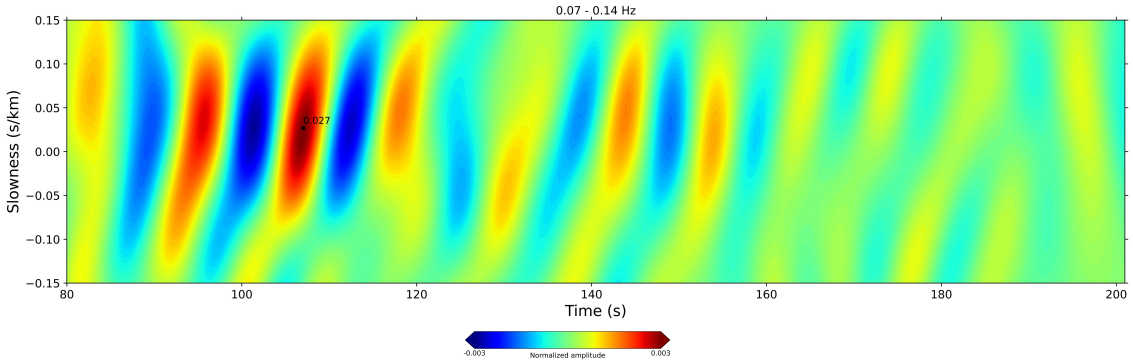

Figure 9: Slowness stack of summer months based on the first 100 km of the causal part of the cross-correlations for the frequency range 0.07–0.15 Hz. Vertical axis gives different slownesses, horizontal axis shows time window in which the mantle transition zone reflections are expected to arrive.

4.4 Directional stacks

The previous stacks included all possible station pairs, containing all possible interstation distances but also all directions between receivers. To retrieve more information on the directions of the incoming wavefronts, directional stacks are shown in this section. Directional stacks are stacks that only contain station pairs in a specific direction. They only contain station pairs where the angle between the intersection line between the stations and a certain reference line lies between 0 and 15°. Figure 10 shows how the seismic array is mainly oriented. The figure indicates that there are more receiver pairs oriented east-west than north-south and the main direction is somewhere between northwest-southeast. The preferred orientation is less prominent for the shorter distances, but still present. Two reference lines are used for the directional stacks: east-west (blue shading in Figure 10) and south-north (green shading in Figure 10). For the east-west stack the most eastern station is taken as the first argument in the cross-correlations, as was done for the previous complete stacks of Figure 5. For the south-north stack, the most southern station is correlated with the most northern one. The causal part thus contains waves travelling from north to south and the acausal part are waves travelling in the opposite direction.

The directional stacks are shown in Figure 11. The east-west stack (Figure 11a) shows clear differences between the acausal and causal parts with respect to the surface waves. They are mainly visible in the acausal part, which is as expected, because there are more surface waves are travelling from west to east, originating at the Pacific ocean located west of California. There are no clear arrivals at 100 and 150 seconds, instead there are arrivals at all times.

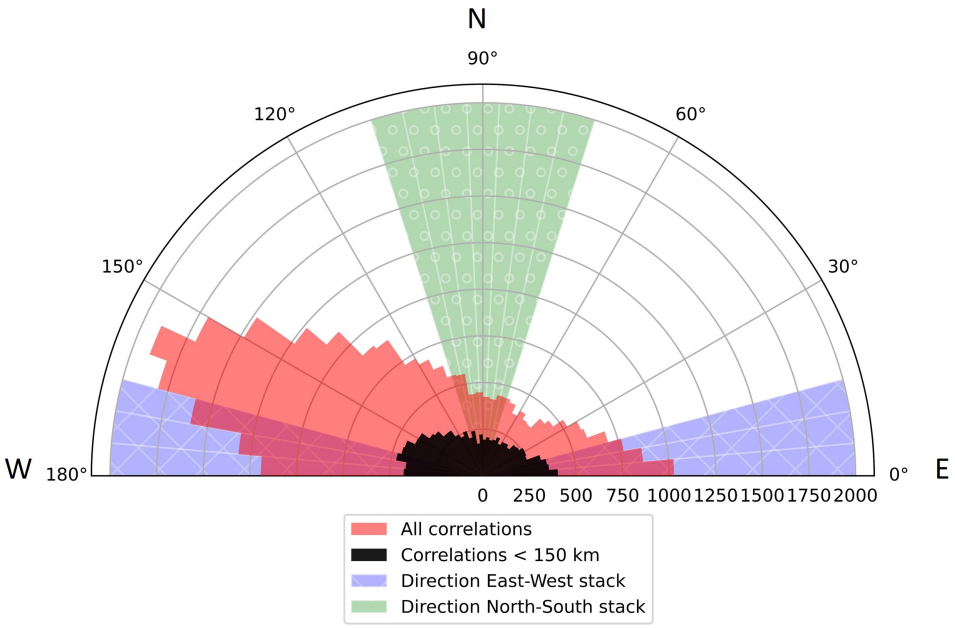

Figure 10: Directions of intersection lines between receivers per 5°. The red bars show the distribution of the angles between the intersection line between all receiver pairs and the East-West direction. The black bars show the same for interstation distances smaller than 150 km, because this is were most mantle zone reflections are observed.

The travel time variations as function of interstation distance are larger than for the summer stack containing all receiver pairs, which indicates larger time delays between stations. The south-north (Figure 11b) stack contains significantly less correlations. There are no receiver pairs with interstation distances longer than 420 km in this stack. The surface waves are more prominent in the acausal part, which are the surface waves travelling from south to north. This is as expected with the Pacific Ocean located south of California. The mantle transition zone reflections are not distinguishable in this stack because of the surrounding arrivals. There are no variations in travel times as function of interstation distances anymore.

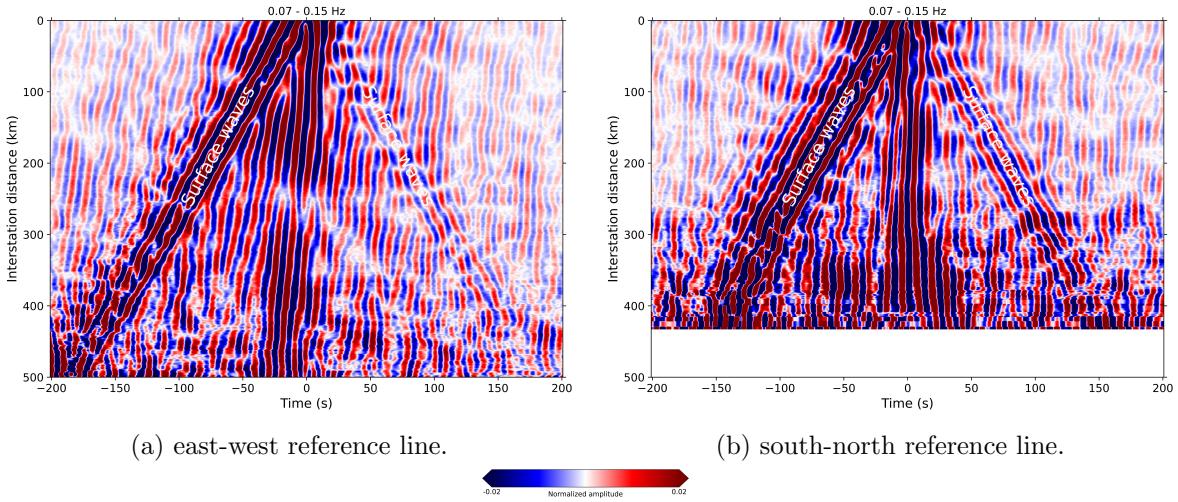

(a) east-west reference line.

(b) south-north reference line.

Figure 11: Two directional stacks based on the summer months (June–Aug.). Stacks only contain station pairs where the angle between the intersection line between the stations and the reference line lies between 0 and 15°.

5 Discussion

The observations on the mantle transition zone reflections are dependent on season, frequency range and interstation distance. The coming sections will elaborate on these dependencies and give possible explanations for different observations.

5.1 Seasonal dependence

The results of the previous section showed that stacking data from all four years into one single stack did not lead to any observable mantle transition zone reflections, independent of the frequency range. This is contrary to what other studies found. Studies of Poli et al. (2012a) (42 stations from January to December 2008), Feng et al. (2017) (198 stations from October 2006 to July 2009), Feng et al. (2019) (526 stations from March 2011 to November 2013) did achieve mantle transition zone reflections when stacking all their data into one single stack. This could be explained by the locations of their seismic arrays, which are all located on cratons. A craton has the advantage of a homogeneous velocity structure which causes time delays at receivers to be primarily caused by differences in travel distance and not by local variations in the velocity structure. The Southern California Seismic Network is located on the Los Angeles Basin, containing highly variable marine and fluvial sediments up to 10 km thick (Hauksson, 1990). Seismic velocity variations in these sediments can affect the interferometry results.

It is also possible that these other studies had a better source region. Seismic interferometry is based on the assumption of a diffuse wavefield, but this is not the case in our study. Microseisms are generated in regions with high oceanic wave heights, these regions are not homogeneously distributed over the earth and also show large seasonal variations. The antipode of the seismic array is located on the edge of a high oceanic wave region, causing the incoming wavefield to have a dominant direction. On top of these arguments, previous studies folded their cross-correlations: they averaged their causal and acausal parts. This is only possible if the cross-correlations are close to symmetric. This is not the case in our study because the wavefield has a dominant direction.

Stacking the data into seasonal stacks significantly improved the results for the summer months, because during these months more usable microseismic noise is generated close to the antipode of the array and less surface waves are created close to the array. Lu et al. (2023) also divided their stacks into seasons and observed similar results, achieving mantle transition zone reflections in summer and not in winter. They did not show their stack containing all data but it is very likely that they required this extra step because their array is located in Italy which is not on a craton either.

5.2 Frequency dependence

Observations on both the four year stack and seasonal stacks are strongly frequency dependent. The appearance of mantle transition zone reflections is restricted to a narrow frequency band in this study: between 0.07–0.15 Hz. This is quite different from other studies, as summarized in Table 1. One explanation could be that the mantle transition zone reflections are primarily caused by incoming PP waves, which generally have lower frequencies than PKP or PKIKP waves because they travel a longer path through the Earth's mantle. However, body waves that have propagated as either P or PP are characterized by slownesses between 0.04–0.1 s/km. The slowness stack in this study resulted in a slowness around 0.025 s/km. Slownesses less than 0.04 s/km likely correspond to PKP core phases (Gerstoft et al., 2008).

Another explanation could be a difference in the mechanism generating the noise at the source. The studies summarized in Table 1 all use the secondary microseism range. In our

Table 1: Frequency bands used in other studies that imaged the mantle transitition zone with ambient seismic noise.

Study:	**Frequency range (Hz)**
Poli et al. (2012a)	0.1–0.5
Feng et al. (2017)	0.1–0.2
Feng et al. (2019)	0.1–0.2
Feng et al. (2021)	0.1–0.5
Pedersen et al. (2023)	0.1–0.4
Lu et al. (2023)	0.1–0.25

study the frequency band lies in between both ranges, also including the primary microseisms, which are created in shallower waters than the secondary microseisms. The antipode of the array is located closely to the Kerguelen plateau, a broad topographic high located in the South Central Indian Ocean. The oceanic plateau extends over 2000 km, between 46 and 64°S, in a northwest-southeast direction towards the Antarctic continental shelf (Munschy & Schlich, 1987). This plateau has been noted by other studies as a significant source of body wave microseisms (Euler et al., 2014). On top of the storm activity there is the enhancing effect of shallow bathymetry, which could possibly be a source for primary microseisms (Reddy et al., 2021).

Another interesting theory that could possibly explain the difference in frequency range is linked to the findings of Zeng & Ni (2010). Their study found a persistent microseism source near the Kyushu Island, Japan. The dominant frequency range of this signal is between 0.07 and 0.12 Hz, which is very similar to the frequency range of this study. Because the range lies between the primary and secondary microseism frequency peaks, the authors suggest that the signals are not necessary caused by ocean waves. A microseism source on land is hard to match with the observations of seasonal dependence of the microseismic noise in this study. However, the noise source from Zeng & Ni (2010) could also be generated from oceanic sources, due to the particular bathymetry near Kyushu Island. The epicentral distance between Kyushu Island and Los Angeles is approximately 85°, which makes it impossible to generate PKP or PKIKP waves between these areas. However, both P and PP waves would be able to travel this path. Their slownesses would then be 0.045 s/km and 0.074 s/km for P or PP waves, respectively (Wang et al., 2018a). This is not in agreement with the slowness that was found. However, because this possible source is located west of California it would mainly create East-West travelling body waves so it is better to approximate the slowness from the East-West stack (Figure 11a). The slowness in this stack is larger than in the total stack and can match with P waves.

5.3 Shape and extent of the mantle transition zone reflections

In the season and frequency range where the mantle transition zone reflections are observed, they are only visible for relatively short interstation distances (< 100 km) and only in the causal part of the correlations. Even then they are still quite hard to distinguish from other signals. First of all, their waveforms appear to be really broad (40 seconds for the P410P and 30 seconds for the P660P). Also, the stacks shows arrivals at most other time differences as well, although with slightly smaller amplitudes. The stacked signal in Figure 8a shows that the P410P has a larger amplitudes than the surrounding signals. This is less evident for the P660P. The reflections are likely only visible at the short distances because at larger distances the effect of velocity heterogeneities starts to play a bigger role, leading to time delays and incoherent stacking. Also, for the P410P, the reflection intersects with the more dominant

surface waves and is therefore not visible anymore. This is especially the case in the acausal part, where surface waves are even more excessive.

In our study, the P410P has larger amplitudes than the P660P (Figure 8a). In the other studies mentioned in Table 1, the P660P also showed slightly smaller amplitudes. The 410 km discontinuity is often observed for low frequency PP data but not for high frequency P'P' data. The 660 km discontinuity is more complex. High frequency P'P' precursors suggest a narrow 660 km discontinuity, while low frequency PP precursor studies often struggle to detect a reflection from the 660 km discontinuity, which is contradictory (Day & Deuss, 2013). Our study coincides with these observations as we see the P410P for low frequencies, but the P660P is not significantly visible in this range.

The broad mantle transition zone reflections in our study could be interpreted with a broad discontinuity. This is not in agreement with previous seismological observations that suggest that the 410 and 660 km discontinuities are sharp (Benz & Vidale, 1993; Vidale et al., 1995). Since other studies (Table 1) observing the mantle transition zone reflections with ambient seismic noise also found broad reflection signals, it is likely an artefact caused by the method used and not due characteristics of the discontinuities, making it complicated to make justifiable interpretations about the mantle transition zone using ambient seismic noise.

5.4 Time delays as function of interstation distance

As mentioned before in the Results section, the mantle transition zone reflections arrive at an inclined angle, the arrival times are not independent of interstation distance and the slowness is not exactly zero. This observation itself is not unusual, as it is likely that waves do not originate exactly at the antipode of the array. In fact, this inclined angle can be explained by the noise source field that is not centered at the antipode. The antipode actually lies on the edge of the noise source field (Figure 6). In the acausal part of the stacks the situation is as expected: for interferometry with a homogeneous, diffuse wavefield, an increasing interstation distance leads to an increasing time difference. This time difference is caused by the longer path the waves travel between stations that are further apart which results in a larger time delay. However, the dependence of time delays on interstation distance of the reflections in the causal parts of the stacks is unexpected. With increasing interstation distance, the time difference decreases. For higher frequencies the arrivals that are still visible have no variations in the travel time delay with interstation distance, which indicates that these higher frequency waves arrive with a smaller incident angle. Possible explanations for these observations will be discussed in the next sections.

5.4.1 Waves arriving out of plane

Seismic interferometry is based on the assumption of a homogeneous, diffuse wavefield. This ideal case is visualized in Figure 12 for horizontally travelling waves in 2D. In this case the cross-correlation leads to a good approximation of the Green's function between the two receivers. The assumption of a homogeneous wavefield is usually not met, resulting in a dominant wavefront with a specific direction arriving at the receivers. This is also the case in our study, as there are clear differences in between the acausal and causal parts of the correlations while for a homogeneous wavefield they would be symmetric. If the dominant wavefront does not exactly arrive in plane with the intersection line between the two receivers, the time difference given by the cross-correlation between these receivers becomes shorter than would be expected for the Green's function, leading to apparent velocities between receivers. Figure 13 illustrates this concept for horizontally travelling waves in 2D. The expected time difference between these two receivers is 4 s, which is achieved either when there is a homogeneous noise field (Figure 12) or when the sources are in line with the receivers (Figure 13a). In the latter

case, the noise sources are located inside the Fresnel zone, which is indicated by the dashed lines, and the cross-correlation results in a perfect reconstruction of the Green's function. If the sources shift outside the Fresnel zone, as in Figures 13b and 13c, the time difference decreases. The cross-correlations now give an apparent time difference which is smaller than the actual time difference, dependent on how the receivers are oriented with respect to noise sources.

A smaller time difference than expected is also what is observed for the mantle transition zone reflections in our study. Even though they are not horizontally travelling waves, the concept still stands. A wavefront reflecting out of plane will lead to an apparent time difference which is smaller than the two way travel time between the receivers. Because the time difference decreases for larger interstation distances, this theory indicates that for larger distances, the source region would move outside the Fresnel zone. It is not likely that the source region varies, but the orientation of the receiver pairs does vary in the array and shifting the orientation of the receivers with respect to the source has the same effect as shifting the source with respect to the receivers (as in Figure 13). It could therefore be that for the longer interstation distances, the orientation of the receivers is gradually moving more out of plane with the sources than for the shorter interstation distances. This can only happen if the longer interstation distances are oriented significantly different from shorter distances.

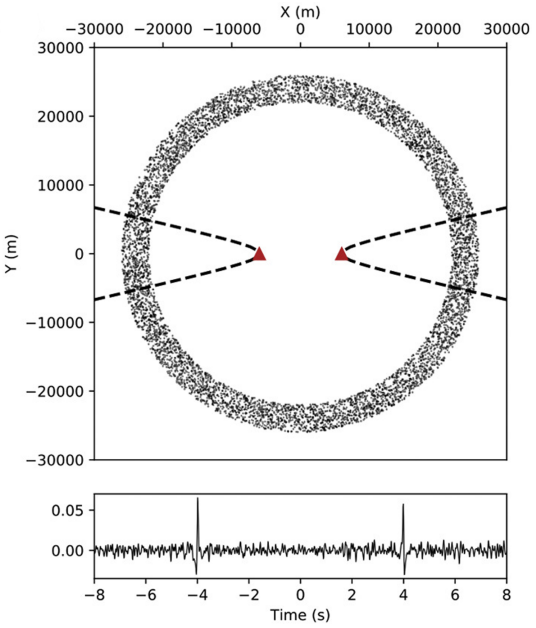

Figure 12: Concept of seismic interferometry for uniformly distributed noise sources around two receivers, and resulting cross-correlation. Dashed lines show Fresnel zone. (Tkalčić et al., 2020)

Figure 10 does indicate that most receiver pairs are oriented northeast-southwest and that this effect is smaller for the shorter distances. This out of plane effect would have to be larger than the counteracting effect of increasing travel times due to longer travel paths between large interstation distance receivers. On top of that, since the decreasing travel times are only observed in the causal part there would have to be a wavefield that lies approximately in plane for east-west correlations (acausal part) and moves out of plane for long distance west-east (causal part) correlations. This is not impossible, as the incoming wavefield is likely very complex due to the broad and variable source region.

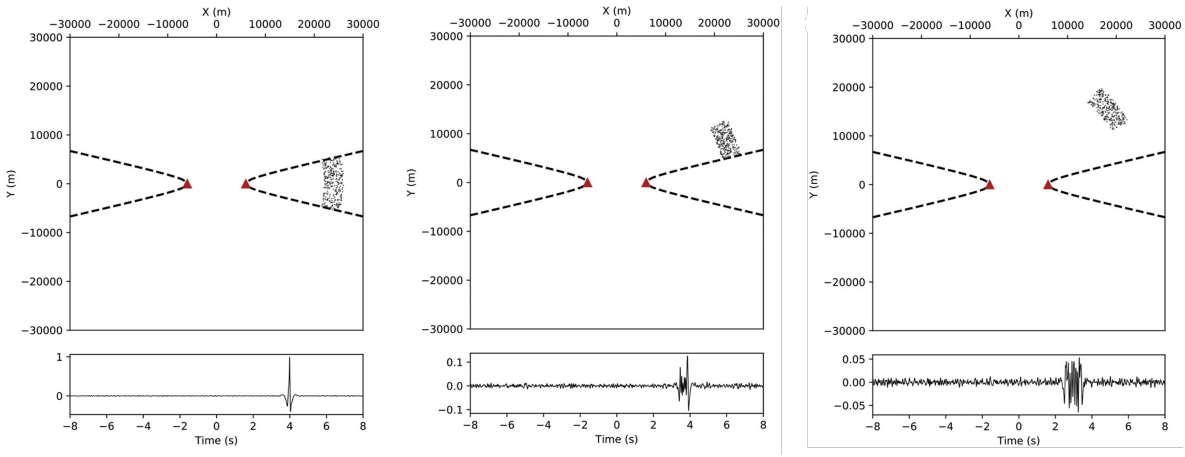

(a) In plane. (b) Slightly out of plane (c) Out of plane

Figure 13: Concept of seismic interferometry for azimuthally-varying distributions of noise sources around two receivers, and resulting cross-correlations. Dashed lines show Fresnel zone. (Tkalčić et al., 2020)

5.4.2 The effect of reflections

Another theory is based on the differences in characteristics of reflecting waves with respect to horizontally travelling waves in cross-correlations. In the case of a homogeneous wavefield, with a receiver pair oriented east-west, horizontally travelling waves observed in the acausal part of a cross-correlation are east-west travelling waves and horizontally travelling waves observed in the causal part are due to west-east travelling waves. In the case where sources are only located east of the receiver pair, there would be no surface waves arrivals in the causal part of the correlation, as illustrated in Figure 14. This concept is also observed in the directional stacks (Figure 11a), where the causal part shows almost no surface waves. For reflections, however, it might also be possible that one wavefront appears on both the causal and acausal parts. This is visualized in Figure 15, which illustrates two situations that can exist for the same incoming wavefront. In the situation of Figure 15a, the direct wave arrives at receiver 1 and the reflected wave at receiver 2. Because the reflected wave takes longer, it will arrive at receiver 2 with a time delay corresponding approximately to the two way travel time of the discontinuity. If the receivers are placed further apart, this time difference will increase. This corresponds with the acausal part of the correlations. The second situation of Figure 15b shows the direct wave arriving at receiver 2 and the reflected wave at receiver 1. The direct wave has a shorter travel path and will thus arrive earlier than the reflected wave, creating

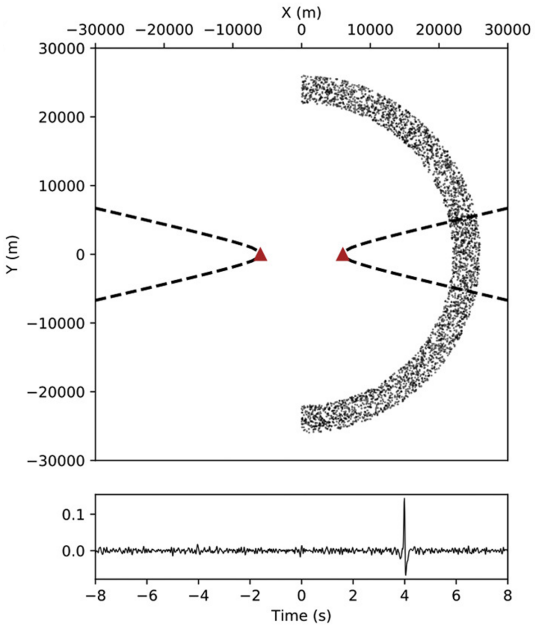

Figure 14: Concept of seismic interferometry for non-uniformly distributed noise sources around two receivers, and resulting cross-correlation. Dashed lines shows Fresnel zone. (Tkalčić et al., 2020)

a time difference. If the receivers are placed further apart, the direct wave will take longer to arrive at the second receiver. Because the direct wave is the first wave to arrive, the time delay will therefore decrease. This situation will appear in the causal part of the correlations because the first arrival is measured at receiver 2. It also explains why the time difference decreases for larger interstation distances.

There are some issues attached to this theory, however. Figure 15 only assumes one wavefront. If there are multiple incoming wavefronts, this will result in multiple travel time differences for the same wavefront, dependent on the angle of the incoming wavefront. To determine if this effect is significant, travel time differences are computed and plotted for different incident angles θ. This is done by first determining the lengths of the different travel paths annotated in Figure 15.

$$\begin{aligned} x &= \frac{d}{\cos(\theta)} \\ y &= 2d\sin(\theta)\tan(\theta) \\ z &= w\sin(\theta) \end{aligned} \tag{5}$$

Where d is the discontinuity depth, w is the interstation distance and θ is the incident angle of the wavefront. For situation of Figure 15a the path difference p and time difference t between the direct and reflected wave is calculated with Equation 6.

$$\begin{aligned} p_{\text{direct}} - p_{\text{reflect}} &= \underbrace{x - (z - y)}_{\text{direct}} - \underbrace{3x}_{\text{reflected}} \\ \Delta p_a &= -2x - z + y \\ \Delta t_a &= \frac{1}{v_p}\left(-2x - z + y\right) \end{aligned} \tag{6}$$

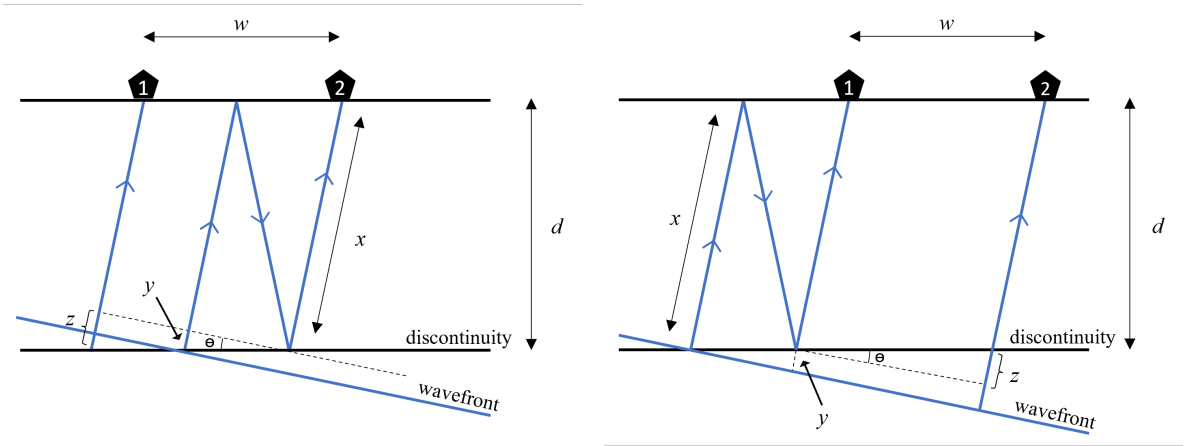

(a) Acausal situation.

(b) Causal situation.

Figure 15: Sketch of a single wavefront arriving at two receivers with interstation distance w as either a direct wave or reflected wave.

The symbols correspond with the annotations in Figure 15: x is one third of the travel path of the reflected wave, y and z are differences in travel path between the direct and the reflected waves due to the incident angle of the wavefront and v_p is the velocity of P waves. For situation Figure 15b the path difference p and time difference t between the reflected and direct wave is calculated with Equation 7.

$$
\begin{aligned}
p_{\text{reflect}} - p_{\text{direct}} &= \underbrace{3x}_{\text{reflected}} - \underbrace{(x+y+z)}_{\text{direct}} \\
\Delta p_b &= 2x - y - z \\
\Delta t_b &= \frac{1}{v_p}\left(2x - y - z\right)
\end{aligned} \tag{7}
$$

The P wave velocity v_p for the 410 km discontinuity calculations will be 8.2 km/s and for the 660 km discontinuity it will be 8.8 km/s. They are chosen different because P wave velocity increases with depth so the average velocity will be higher for a wave that has reflected on the 660 km discontinuity. These travel times are computed for different interstation distances w and different incident angles θ.

Figure 16 shows the results for $\theta = 10°$. The vertical axis shows interstation distances up to 150 km, because this is where the reflections are best observed. The horizontal axis shows the time window where the P410P and P660P are expected to arrive, Figure 16a for the acausal part and Figure 16b for the causal part. The figure shows that a single wavefront arriving from the east gives orientations of the reflections that are in agreement with the observations of out study: in the acausal part the time difference increases with interstation distance and in the causal part it decreases. The assumption of a wavefront mainly arriving from a specific direction is not unrealistic, as it is dependent on the location of the source. It could possibly even explain the observations on the directional stack in Figure 11. The east-west stack showed large travel time distances while the south-north stack did not. This could be explained by a wavefront mainly arriving from the west, because this is perpendicular to the north-south directions travel time differences will be minimal due to the out of plane principle. However, it is likely that the noise originates from a source region, so a single wavefront might not be a valid assumption. Figure 17 therefore shows the results for incident angles between 5° and 20°, with the acausal times in Figure 17a and the causal times in 17b.

The figure indicates that multiple incident angles could result in broad reflections, in accordance with our results. Also, the reflections would narrow for larger interstation distances in the acausal part and broaden in the causal part. This could possibly explain why the mantle transition zone reflections are only observed for small interstation distances in the causal part of the correlation, for larger interstation distances the different incident angles can cause incoherent stacking. The extent of broadening and narrowing depends on the minimum and maximum incident angle of the incoming wavefronts. This narrowing and broadening not very clearly observed in the results of our study, which could indicate a narrow range of incident angles.

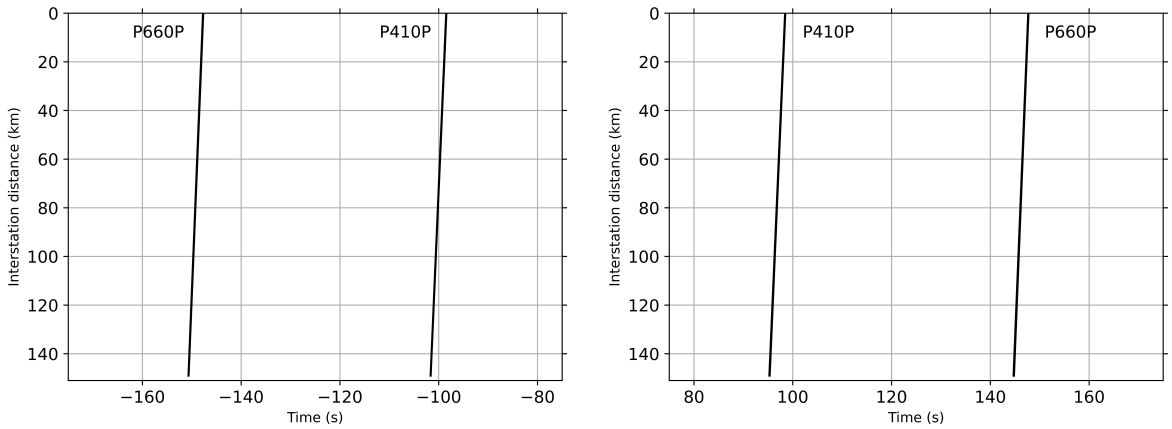

(a) Acausal part. (b) Causal part

Figure 16: Travel time difference as function of interstation distance for single wavefront with an incident angle of 10° for the P410P and P660P. Vertical axis shows interstation distances up to 150 km. Horizontal axis shows the time window in which mantle transition zone reflections are expected to arrive.

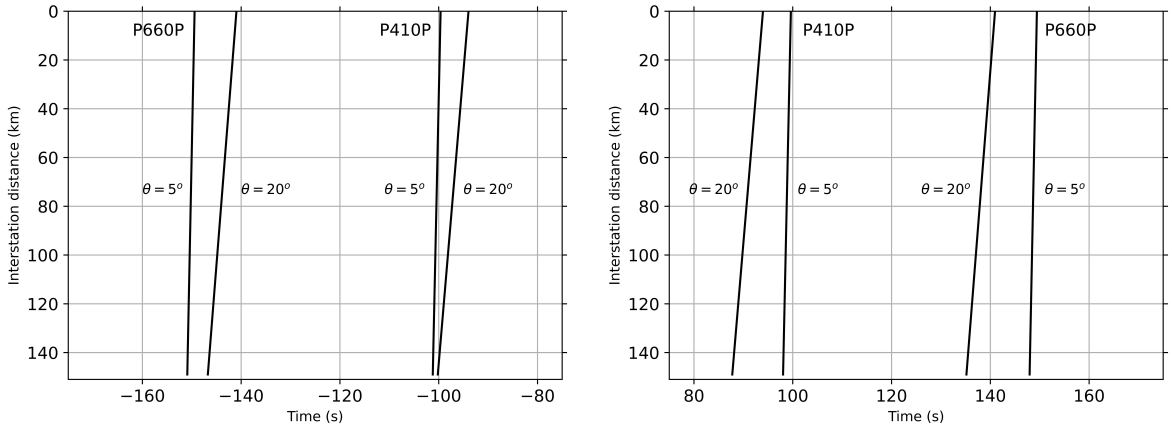

(a) Acausal part. (b) Causal part

Figure 17: Travel time difference as function of interstation distance for wavefronts with incident angles between 5° and 20° for the P410P and P660P. Vertical axis shows interstation distances up to 150 km. Horizontal axis shows the time window in which mantle transition zone reflections are expected to arrive.

5.5 Improvements and recommendations

Our study could possibly be improved by adding more data. For example, more receivers could be added by also involving the Northern California Seismic Network. Furthermore, additional years of data could be downloaded to further improve signal-to-noise ratios.

Improving the understanding of the results and working towards interpreting them could be done by determining the source region of the noise. This will allow us to distinguish between the previously mentioned theories and speculations. This could be done with beamforming, a method that uses the differential travel times of the wavefront due to not only a specific slowness but also a specific back azimuth (Rost & Thomas, 2002). Constructive stacking will happen if recordings are appropriately shifted in time for a certain back azimuth and

slowness. The combination of backazimuth and slowness will give information about the sources of different phases which may help explain the results better.

Although there are limitations caused by the specific locations and time window of earthquakes, detailed interpretations about the mantle transition zone reflections are more trustworthy with earthquake based imaging methods. With these methods the source region is already known from the start and no fundamental assumptions are violated as is the case for a nonhomogeneous wavefield in seismic interferometry.

6 Conclusions

Our study showed that mantle transition zone reflections from the 410 and 660 km discontinuities can be retrieved with microseismic noise in California. The observed signals show both frequency and seasonal dependence, indicating that the microseismic noise source field is highly variable. The best reflections were observed between June and August in the frequency range of 0.07–0.15 Hz, including both the primary and secondary microseisms. In these most useful microseismic noise is generated in the Southern Ocean, close to the antipode of the seismic array. The reflection of the 410 discontinuity has larger amplitudes than the reflection of the 660 km discontinuity, agreeing with earlier studies struggling to the detect the 660 km discontinuity with PP waves in this lower frequency range.

In our study we are dealing with a nonhomogeneous wavefield, violating the assumption seismic interferometry is based on and causing the cross-correlation to be a poor approximation of the Green's function. Previous studies using ambient seismic noise to image the mantle transition zone did not consider this while making their interpretations.

A Seasonal stacks for all frequency ranges

A.1 Spring

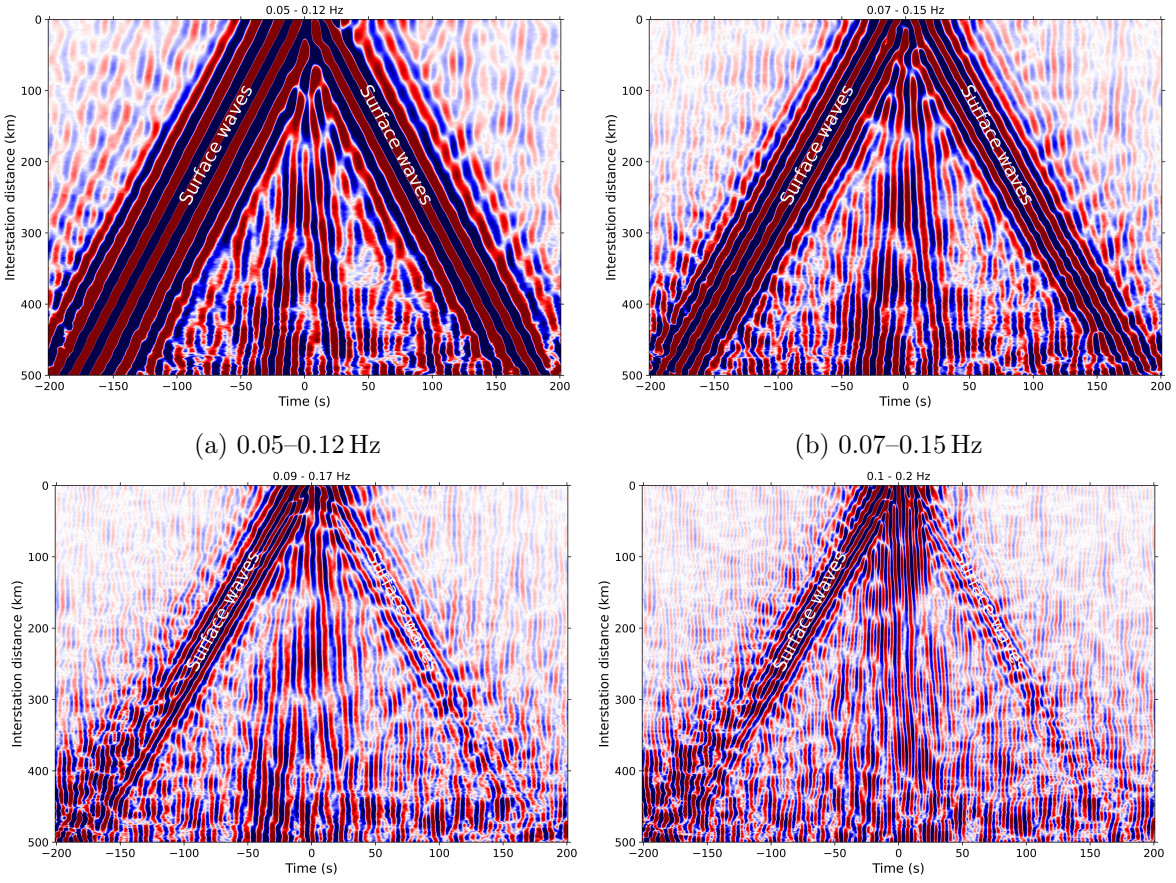

(a) 0.05–0.12 Hz

(b) 0.07–0.15 Hz

(c) 0.09–0.17 Hz

(d) 0.1–0.2 Hz

Figure 18: Spring stacks of the cross-correlations arranged by interstation distance on the vertical axis for all frequency ranges.

A.2 Summer

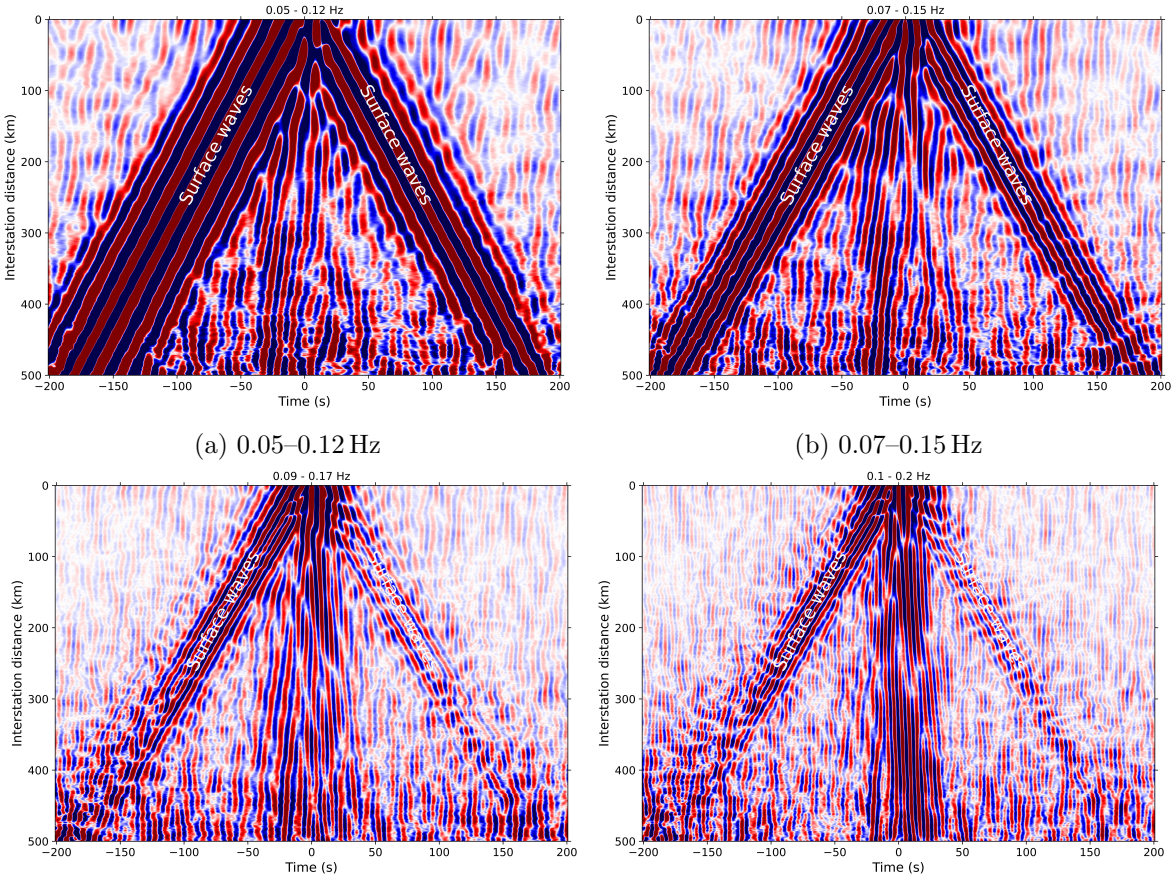

(a) 0.05–0.12 Hz

(b) 0.07–0.15 Hz

(c) 0.09–0.17 Hz

(d) 0.1–0.2 Hz

Figure 19: Summer stacks of the cross-correlations arranged by interstation distance on the vertical axis for all frequency ranges.

A.3 Autumn

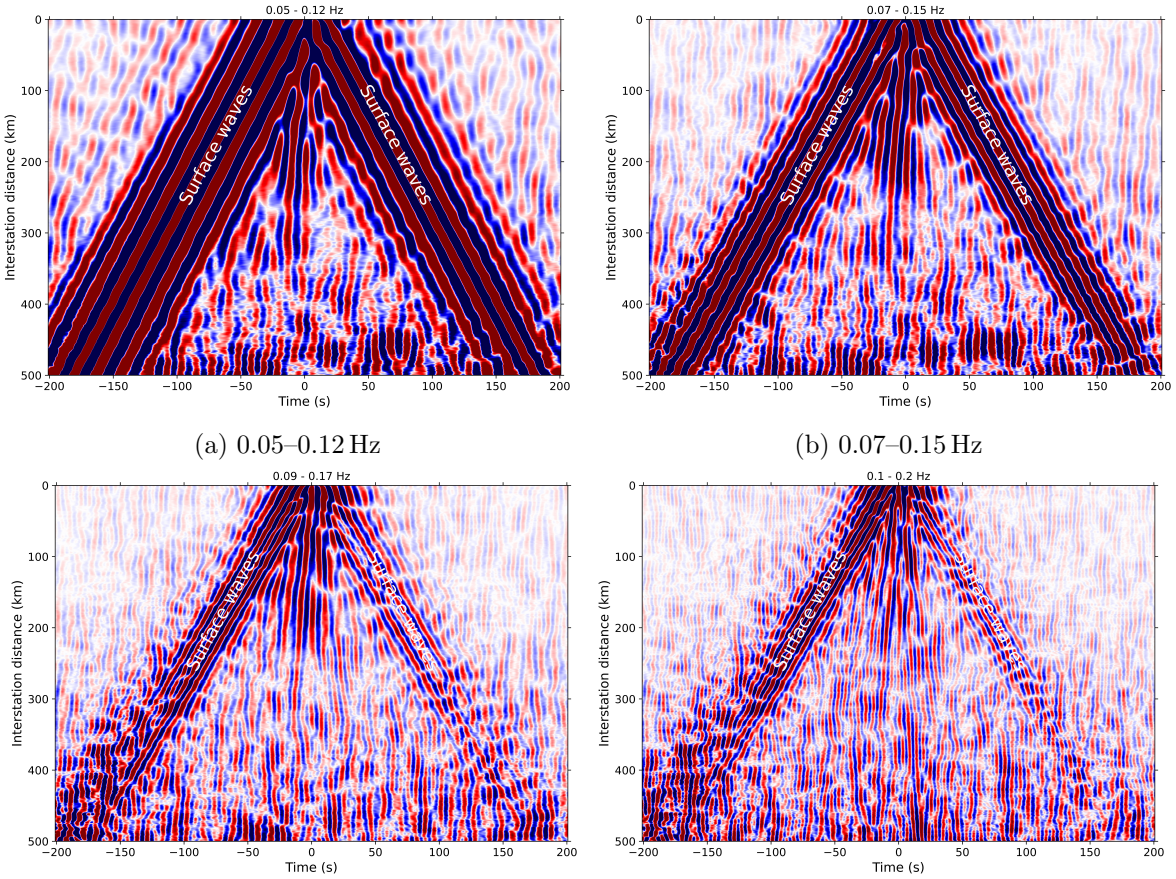

(a) 0.05–0.12 Hz

(b) 0.07–0.15 Hz

(c) 0.09–0.17 Hz

(d) 0.1–0.2 Hz

Figure 20: Autumn stacks of the cross-correlations arranged by interstation distance on the vertical axis for all frequency ranges.

A.4 Winter

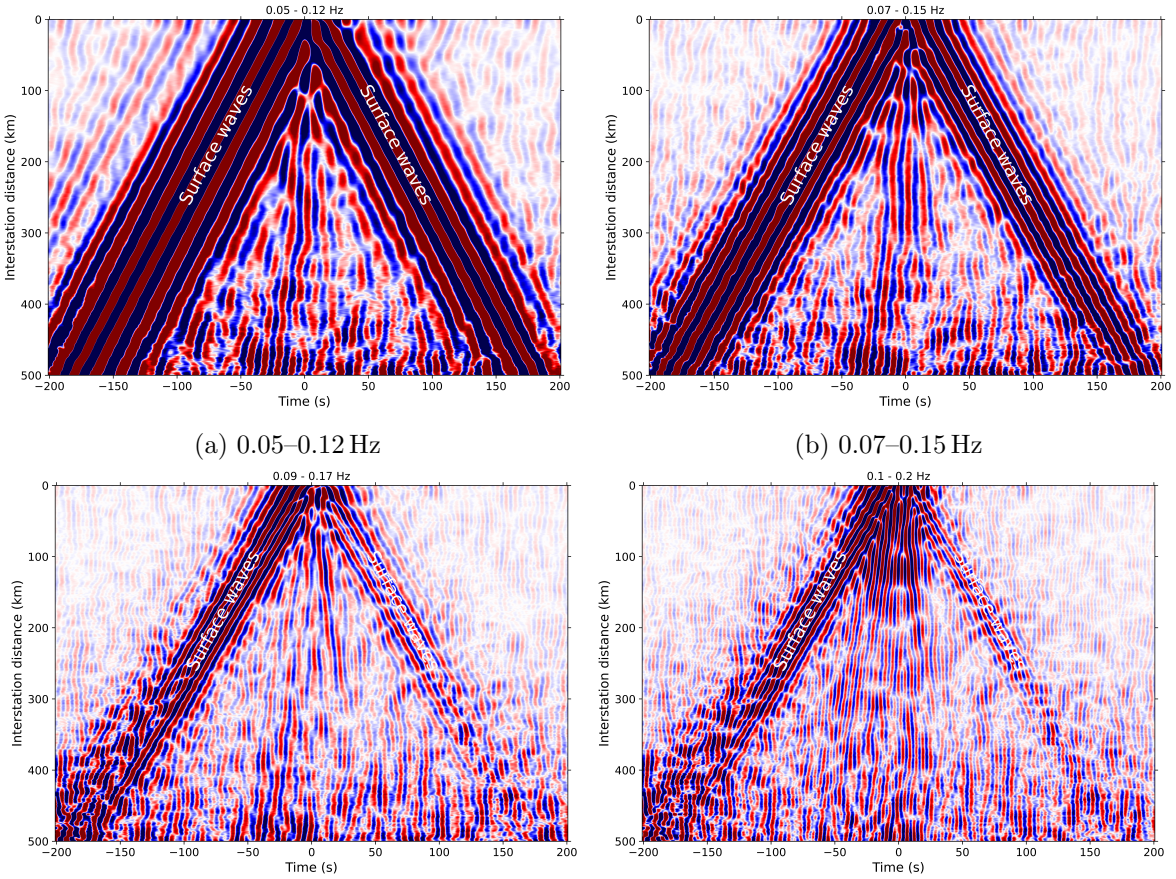

(a) 0.05–0.12 Hz

(b) 0.07–0.15 Hz

(c) 0.09–0.17 Hz

(d) 0.1–0.2 Hz

Figure 21: Winter stacks of the cross-correlations arranged by interstation distance on the vertical axis for all frequency ranges.

References

Ammon, C. J., Velasco, A. A., Lay, T., & Wallace, T. C. (2020). *Foundations of modern global seismology*. Academic Press.

Bensen, G., Ritzwoller, M., Barmin, M., Levshin, A. L., Lin, F., Moschetti, M., Shapiro, N., & Yang, Y. (2007). Processing seismic ambient noise data to obtain reliable broad-band surface wave dispersion measurements. *Geophysical journal international*, 169(3), 1239–1260.

Benz, H. & Vidale, J. (1993). Sharpness of upper-mantle discontinuities determined from high-frequency reflections. *Nature*, 365(6442), 147–150.

Boué, P., Poli, P., Campillo, M., Pedersen, H., Briand, X., & Roux, P. (2013). Teleseismic correlations of ambient seismic noise for deep global imaging of the Earth. *Geophysical Journal International*, 194(2), 844–848.

California Institute of Technology and United States Geological Survey Pasadena (1926). Southern California Seismic Network.

Chevrot, S., Vinnik, L., & Montagner, J.-P. (1999). Global-scale analysis of the mantle Pds phases. *Journal of Geophysical Research: Solid Earth*, 104(B9), 20203–20219.

CMEMS (2024). Global ocean waves reanalysis. https://doi.org/10.48670/moi-00022. Accessed: 2024-10-01.

Day, E. A. & Deuss, A. (2013). Reconciling PP and P 'P 'precursor observations of a complex 660 km seismic discontinuity. *Geophysical Journal International*, 194(2), 834–838.

Deuss, A. (2009). Global observations of mantle discontinuities using SS and PP precursors. *Surveys in geophysics*, 30, 301–326.

Draganov, D., Campman, X., Thorbecke, J., Verdel, A., & Wapenaar, K. (2009). Reflection images from ambient seismic noise. *Geophysics*, 74(5), A63–A67.

Euler, G. G., Wiens, D. A., & Nyblade, A. A. (2014). Evidence for bathymetric control on the distribution of body wave microseism sources from temporary seismic arrays in Africa. *Geophysical Journal International*, 197(3), 1869–1883.

Feng, J., Yao, H., Poli, P., Fang, L., Wu, Y., & Zhang, P. (2017). Depth variations of 410 km and 660 km discontinuities in eastern North China craton revealed by ambient noise interferometry. *Geophysical Research Letters*, 44(16), 8328–8335.

Feng, J., Yao, H., & Wang, W. (2019). Imaging mantle transition zone discontinuities in southwest China from dense array ambient noise interferometry. *Earthquake Science*, 31(5-6), 301–310.

Feng, J., Yao, H., Wang, Y., Poli, P., & Mao, Z. (2021). Segregated oceanic crust trapped at the bottom mantle transition zone revealed from ambient noise interferometry. *Nature Communications*, 12(1), 2531.

Gerstoft, P., Shearer, P. M., Harmon, N., & Zhang, J. (2008). Global P, PP, and PKP wave microseisms observed from distant storms. *Geophysical Research Letters*, 35(23).

Hauksson, E. (1990). Earthquakes, faulting, and stress in the Los Angeles basin. *Journal of Geophysical Research: Solid Earth*, 95(B10), 15365–15394.

Helffrich, G. R. & Wood, B. J. (2001). The Earth's mantle. *Nature*, 412(6846), 501–507.

Hoffman, P. F. (1988). United plates of America, the birth of a craton: Early proterozoic assembly and growth of laurentia. *Annual Review of Earth and Planetary Sciences*, 16(1), 543–603.

Landès, M., Hubans, F., Shapiro, N. M., Paul, A., & Campillo, M. (2010). Origin of deep ocean microseisms by using teleseismic body waves. *Journal of Geophysical Research: Solid Earth*, 115(B5).

Li, C., van der Hilst, R. D., Engdahl, E. R., & Burdick, S. (2008). A new global model for P wave speed variations in earth's mantle. *Geochemistry, Geophysics, Geosystems*, 9(5).

Lin, F.-C., Ritzwoller, M. H., & Snieder, R. (2009). Eikonal tomography: surface wave tomography by phase front tracking across a regional broad-band seismic array. *Geophysical Journal International*, 177(3), 1091–1110.

Lu, Y., Pedersen, H. A., Stehly, L., & Group, A. W. (2022). Mapping the seismic noise field in Europe: spatio-temporal variations in wavefield composition and noise source contributions. *Geophysical Journal International*, 228(1), 171–192.

Lu, Y., Schmid, S. M., Wang, Q.-Y., & Bokelmann, G. (2023). Mapping the mantle transition zone discontinuities across South-Central Europe using body waves from seismic noise correlations. *Earth and Planetary Science Letters*, 624, 118457.

Munschy, M. & Schlich, R. (1987). Structure and evolution of the Kerguelen-Heard Plateau (Indian Ocean) deduced from seismic stratigraphy studies. *Marine Geology*, 76, 131–152.

Nishida, K. & Takagi, R. (2016). Teleseismic S wave microseisms. *Science*, 353(6302), 919–921.

Pedersen, H. A., Mattern, F., Poli, P., & Stehly, L. (2023). Imaging with seismic noise: improving extraction of body wave phases from the deep earth through selective stacking based on H/V ratios. *Geophysical Journal International*, 232(2), 1455–1467.

Peterson, J. R. (1993). *Observations and modeling of seismic background noise*. Technical report, US Geological Survey.

Poli, P., Campillo, M., Pedersen, H., & Group, L. W. (2012a). Body-wave imaging of Earth's mantle discontinuities from ambient seismic noise. *Science*, 338(6110), 1063–1065.

Poli, P., Pedersen, H., & Campillo, M. (2012b). Emergence of body waves from cross-correlation of short period seismic noise. *Geophysical Journal International*, 188(2), 549–558.

Reading, A. M., Koper, K. D., Gal, M., Graham, L. S., Tkalčić, H., & Hemer, M. A. (2014). Dominant seismic noise sources in the Southern Ocean and West Pacific, 2000–2012, recorded at the Warramunga Seismic Array, Australia. *Geophysical research letters*, 41(10), 3455–3463.

Reddy, T. R., Dewangan, P., Bhaskaran, P. K., & Roy, P. N. S. (2021). Possible linkages between microseisms in the Andaman-Nicobar region and swells in the South Indian Ocean. *Seismological Society of America*, 92(2A), 1052–1068.

Revenaugh, J. & Jordan, T. H. (1991). Mantle layering from ScS reverberations: 2. The transition zone. *Journal of Geophysical Research: Solid Earth*, 96(B12), 19763–19780.

Rost, S. & Thomas, C. (2002). Array seismology: Methods and applications. *Reviews of geophysics*, 40(3), 2–1.

Roux, P., Sabra, K. G., Gerstoft, P., Kuperman, W., & Fehler, M. C. (2005). P-waves from cross-correlation of seismic noise. *Geophysical Research Letters*, 32(19).

Ruigrok, E., Campman, X., & Wapenaar, K. (2011). Extraction of P-wave reflections from microseisms. *Comptes Rendus Geoscience*, 343(8-9), 512–525.

Sabra, K. G., Gerstoft, P., Roux, P., Kuperman, W., & Fehler, M. C. (2005). Surface wave tomography from microseisms in Southern California. *Geophysical Research Letters*, 32(14).

Schimmel, M. & Paulssen, H. (1997). Noise reduction and detection of weak, coherent signals through phase-weighted stacks. *Geophysical Journal International*, 130(2), 497–505.

Shapiro, N. M. & Campillo, M. (2004). Emergence of broadband rayleigh waves from correlations of the ambient seismic noise. *Geophysical Research Letters*, 31(7).

Shearer, P. M. & Masters, T. G. (1992). Global mapping of topography on the 660-km discontinuity. *Nature*, 355(6363), 791–796.

Sorrells, G., McDonald, J. A., Der, Z., & Herrin, E. (1971). Earth motion caused by local atmospheric pressure changes. *Geophysical Journal International*, 26(1-4), 83–98.

Stehly, L., Campillo, M., & Shapiro, N. (2006). A study of the seismic noise from its long-range correlation properties. *Journal of Geophysical Research: Solid Earth*, 111(B10).

Suslick, K. S. (2001). Encyclopedia of physical science and technology. *Sonoluminescence and sonochemistry, 3rd edn. Elsevier Science Ltd, Massachusetts*, (pp. 1–20).

Tanimoto, T. & Anderson, A. (2023). Seismic noise between 0.003 Hz and 1.0 Hz and its classification. *Progress in Earth and Planetary Science*, 10(1), 56.

Tanimoto, T., Ishimaru, S., & Alvizuri, C. (2006). Seasonality in particle motion of microseisms. *Geophysical Journal International*, 166(1), 253–266.

Tkalčić, H., Phạm, T.-S., & Wang, S. (2020). The Earth's coda correlation wavefield: Rise of the new paradigm and recent advances. *Earth-Science Reviews*, 208, 103285.

Vidale, J. E., Ding, X.-Y., & Grand, S. P. (1995). The 410-km-depth discontinuity: A sharpness estimate from near-critical reflections. *Geophysical research letters*, 22(19), 2557–2560.

Wang, W., Gerstoft, P., & Wang, B. (2018a). Interference of teleseismic body waves in noise cross-correlation functions in Southwest China. *Seismological Research Letters*, 89(5), 1817–1825.

Wang, W., Gerstoft, P., & Wang, B. (2018b). Seasonality of p wave microseisms from NCF-based beamforming using chinarray. *Geophysical Journal International*, 213(3), 1832–1848.

Wapenaar, K., Draganov, D., Snieder, R., Campman, X., & Verdel, A. (2010). Tutorial on seismic interferometry: Part 1—basic principles and applications. *Geophysics*, 75(5), 75A195–75A209.

Yao, H. & Van Der Hilst, R. D. (2009). Analysis of ambient noise energy distribution and phase velocity bias in ambient noise tomography, with application to SE Tibet. *Geophysical Journal International*, 179(2), 1113–1132.

Zeng, X. & Ni, S. (2010). A persistent localized microseismic source near the Kyushu Island, Japan. *Geophysical Research Letters*, 37(24).

Zhan, Z., Ni, S., Helmberger, D. V., & Clayton, R. W. (2010). Retrieval of moho-reflected shear wave arrivals from ambient seismic noise. *Geophysical Journal International*, 182(1), 408–420.